Advances in Nano Research, *Vol. 17, No.4 (2024) 369-383*
https://doi.org/10.12989/anr.2024.17.4.369

Optimization of intelligent prosthetic hands using artificial neural networks and nanoscale technologies for enhanced performance

Jialing Li[1], Gongxing Yan[*2], Zefang Wang[1], Belgacem Bouallegue[3] and Tamim Alkhalifah[4]

[1]*School of Artificial intellegence, Chongqing Youth Vocational & Technical College; Chongqing 401320, China*
[2]*Luzhou vocational and technical college, Luzhou 646000, Sichuan, China*
[3]*Department of Computer Engineering, College of Computer Science, King Khalid University, ABHA, 61421, Saudi Arabia*
[4]*Department of Computer Engineering, College of Computer, Qassim University, Buraydah, Saudi Arabia*

(*Received August 21, 2021, Revised October 7, 2024, Accepted October 8, 2024*)

Abstract. Annular nano-electromechanical systems (NEMS) in intelligent prosthetic hands enhance precision by serving as highly sensitive sensors for detecting pressure, vibrations, and deformations. This improves feedback and control, enabling users to modulate grip strength and tactile interaction with objects more effectively, enhancing prosthetic functionality. This research focuses on the electro-thermal buckling behavior of multi-directional poroelastic annular NEMS used as temperature sensors in airplanes. In the present study, thermal buckling performance of nano-scale annular functionally graded plate structures integrated with piezoelectric layers under electrical and extreme thermal loadings is investigated. In this regard, piezoelectric layers are placed on a disk made of metal matrix composite with graded properties in three radials, thickness and circumferential directions. The grading properties obey the power-law distribution. The whole structure is embedded in thermal environment. To model the mechanical behavior of the structure, a novel four-variable refined quasi-3D sinusoidal shear deformation theory (RQ-3DSSDT) is engaged in obtaining displacement field in the whole structure. The validity of the results is examined by comparing to a similar problem published in literature. The results of the buckling behavior of the structure in different boundary conditions are presented based on the critical temperature rise and critical external voltage. It is demonstrated that increase in the nonlocal and gradient length scale factor have contradicting effects on the critical temperature rise. On the other hand, increase in the applied external voltage cause increase in the critical temperature. Effects of other parameters like geometrical parameters and grading indices are presented and discussed in details.
Keywords: annular sector nanodisk; artificial intelligence; electro-thermal buckling; finite difference method; prosthetic hands

1. Introduction

Extreme thermal conditions are inevitable in many industrial and engineering applications (Drai *et al*. 2023, Esen *et al*. 2023, Zhang *et al*. 2023, 2024, Eghbali and Hosseini 2024, Ghazwani *et al*. 2024). The role of the design engineer is to predict the thermal condition as well as the response of the structures in these conditions. The considerations should take in account the material properties change, variation in geometry and dimension of the structure and the forces applied to the structure due to rise in the temperature. Variations in these conditions cause changes in the structural behavior or even induce instability under dynamic and static loading conditions. In this regard, many attempts have been devoted to the analyzing, prediction and controlling of instability in different structural member specifically in small scales. One of the applications of temperature sensors in intelligent prosthetic hands is shown in Fig. 1.

One of the most notable methods of controlling structures is integrating piezoelectric material in structures to generate additional force in a smart way. Burdess and Fawcett (1992), as one of the pioneering studies in controlling structures using piezoelectric materials, utilized electrical voltage to control free and forced vibration of a cantilever beam. The control procedure was based on the acceleration measurement of the beam and applying proper voltage to control vibration. Kargarnovin *et al*. (2007) used piezoelectric patches as both motion sensor and controlling device in vibration control of the functionally graded (FG) plate structure. They modeled the simply supported plate with classical plate theory and analytically solved the equations of motions using Fourier analysis. The results of their study showed that increasing the feedback gain in the control system substantially decreased both amplitude and frequency of the plate. Moreover, increase in the FG characteristics cause decrease in the vibrational properties of the plate structures. Shivashankar and Gopalakrishnan (2020) reviewed using of piezoelectric layers in controlling vibrations of different structures. The active vibration control was the center of investigation using piezoelectric patches. The position, thickness and other properties are crucial in efficacy of using piezoelectric layers for the aim of controlling systems. Using PD controller in piezoelectric patches, Zhang *et al*. (2021) succeeded in controlling vibration in a rotating cylindrical shell conveying fluids. They employed GDQM to solve the governing equations

*Corresponding author, Ph.D.,
E-mail: yaaangx@126.com

ISSN: 2287-237X (Print), 2287-2388 (Online)

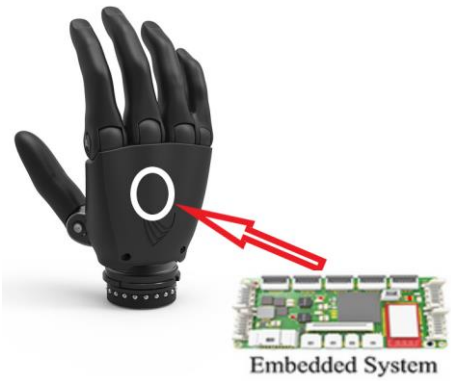

Fig. 1 One of the applications of temperature sensors in intelligent prosthetic hands

obtained using nonlocal stress-strain gradient theory. Their calculations showed the effects of geometry, material properties and fluid velocity on the stability of the structure. Chung *et al*. (2012) utilized piezoelectric patches to measure the responses of a column under compressive dynamic loading. The piezoelectric patches have both sensing and actuating tasks in many applications. A review of geopolymer with addition of graphene oxide towards sustainable construction materials was presented by Apandi *et al*. (2024).

Temperature condition in environment also effects the buckling behavior of a structure. Shahsiah and Eslami (2003) presented a methodology to show the effects of temperature change in buckling of a cylindrical shell structure. The first-order shear deformation theory along with Sanders equations were utilized to obtain the displacement field of the shell structure. On the other hand, a linear graduation of material properties change is considered. The results were presented for the case of simply supported cylindrical shell structure and different thermal situations. The equations were solved analytically and the results indicated considerable effect of thermal environment condition on the buckling of functionally graded shell structure. Al-shujairi and Mollamahmutoğlu (2018) considered the effects of temperature on free vibrational and buckling responses of a FG micro-beam structure. Higher-order shear deformation theory in conjunction with nonlocal strain gradient theory were utilized to relate the stress component to displacement of the shell structure. The equations of motion and equilibrium equations were obtained using Hamilton's principle and solve using numerical methods. The results showed that elastic foundation of the beam, temperature and nonlocal effects had the great effects on the buckling critical loads of the structure.

A composite structure is an engineered material system made by combining two or more distinct materials to achieve superior properties that cannot be obtained from any of the individual components alone (Wang *et al*. 2023, Zhang *et al*. 2024). Typically, one material serves as the matrix, which binds and protects the reinforcing fibers or particles, while the other acts as the reinforcement, providing strength and stiffness (Lv *et al*. 2024, Wang *et al*. 2024). Common matrix materials include polymers, metals, and ceramics, while fibers can be made of materials such as carbon, glass, or aramid (Hirao *et al*. 2023, Sun *et al*. 2024). The combination of these materials allows composite structures to be lightweight yet highly durable, making them ideal for applications where strength-to-weight ratio is crucial (Liu *et al*. 2020, Yang *et al*. 2023). The design flexibility of composite structures allows engineers to tailor their properties to specific load requirements (Yang *et al*. 2022, 2023). This is achieved by varying the type, orientation, and distribution of the reinforcing fibers within the matrix (Chen *et al*. 2023, Song *et al*. 2024). Composite structures are widely used in aerospace, automotive, marine, and civil engineering applications due to their enhanced performance under load, resistance to corrosion, and ability to withstand harsh environmental conditions (Hu *et al*. 2023, Wu *et al*. 2023). One of the key advantages is that composites can be designed to exhibit anisotropic properties, meaning their mechanical properties vary in different directions, which is particularly useful in optimizing structural performance (Han *et al*. 2023a, b). Additionally, composites often have superior fatigue resistance compared to traditional materials like metals (Liu *et al*. 2021, Taheri *et al*. 2021). Advanced composite structures, such as those reinforced with nanomaterials, are gaining attention for their enhanced mechanical, thermal, and electrical properties (Taheri *et al*. 2020, Feng *et al*. 2021). These composites, which include nano-sized fillers like graphene, carbon nanotubes, or nanoclays, have potential applications in next-generation structural systems (Firouzianhaji *et al*. 2021, Mehrabi *et al*. 2021). Despite their numerous advantages, composite structures require careful manufacturing techniques to avoid defects, such as voids or fiber misalignment, which can compromise their mechanical integrity (Taheri *et al*. 2019, Mehrabi *et al*. 2021). Ongoing research is focused on improving fabrication methods, optimizing material selection, and enhancing the durability of composite structures to meet the demands of increasingly complex engineering challenges (Toghroli *et al*. 2020).

Ref. (Qiu and Wang 2024) explored the use of advanced algorithms to categorize credit card users based on their financial behavior, aiming to enhance economic stability through more targeted financial strategies and risk management. Ref. (Qiu 2019) focused on advanced statistical methods for estimating the risk of rare but impactful financial losses, employing extreme value theory combined with mixture models to better capture and assess tail risks in financial markets.

Wang considered the buckling capacity improvement in the columns by attaching piezoelectric layers and applying voltage to the beam (Wang 2002). The result of the study demonstrated the effective application of voltage and optimized position of the piezoelectric layer on the postponing linear buckling of columns. Nonlinear buckling and post-buckling of multi-layer plates made with functionally graded nanocomposites were the subject of the study by Wu *et al*. (2017). The FG material were modeled using different concentration of graphene platelets in matrix in each layer. Numerical analyses demonstrated the substantial variation in the buckling and post-buckling behavior of the plate structure due to different distribution patterns of the layers. Moreover, the post-buckling and buckling of the FSDT plate were highly dependent on the in-plane force measure. Safarpour *et al*. (2019) provided an exact solution for the size-dependent buckling and natural

frequency of cylindrical composite structures engaging modified couple stress theory. The effects of functionally graded pattern and thermal condition on the linear buckling of the shell structure were presented and discussed in detail. In a similar analysis, Ebrahimi *et al*. (2020) incorporated porosity in the thermal buckling response of cylindrical nano-composite structure. It was revealed that increase in the porosity of the FG material deteriorate the buckling capacity of the structure. The buckling critical force and critical temperature of doubly-curved panel structure were examined in an article by Moayedi *et al*. (Moayedi *et al*. 2020). High-order shear deformation theory and nonlocal strain gradient theory were employed in revealing effects of different geometrical and loading conditions on the thermal buckling state. Sepahi *et al*. (2011) employed nonlinear theory to obtain thermal buckling of annular nano-scale plate structures. In their analysis, the thermal properties of the materials were considered to be temperature-dependent and DQM numerical solution were applied to in extracting parametric results. The outcome of the study indicated that the variation of the material properties due to change in temperature could effectively influence the buckling critical condition and post-buckling deformation state.

This study provides a comprehensive analysis of the electro-thermal buckling behavior of multi-directional poroelastic NEMS used as temperature sensors in airplanes. The research emphasizes the critical role of electro-thermal loads in influencing the stability and performance of these advanced sensors. It is for the first time that thermal buckling performance of nano-scale annular functionally graded plate structures integrated with piezoelectric layers under electrical and extreme thermal loadings with a novel four-variable refined quasi-3D sinusoidal shear deformation theory (RQ-3DSSDT) is investigated. In this regard, piezoelectric layers are placed on a disk made of metal matrix composite with graded properties in three radials, thickness and circumferential directions. The grading properties obey the power-law distribution. The whole structure is embedded in thermal environment. To model the mechanical behavior of the structure, a novel four-variable refined quasi-3D sinusoidal shear deformation theory (RQ-3DSSDT) is engaged in obtaining displacement field in the whole structure. In addition, nonlocal strain gradient theory (NSGT) is used to correlate stress tensor to strain tensor. The equilibrium equations of the structure is extracted employing minimum virtual work principle and solved by the two-dimensional discrete singular convolution method (2D-DSCM). The validity of the results is examined by comparing to a similar problem published in literature. The results of the buckling behavior of the structure in different boundary conditions are presented based on the critical temperature rise and critical external voltage. The results of the present study could be used by scientists and engineers in the field of nano-scale structural mechanics.

2. Effective material properties

2.1 Multi-directional functionally graded materials (MD-FGMs)

Temperature dependent material properties of FGMs are mathematically modeled with power-law relations. For the case of the MD-FGMs, the power-law relation is described below:

$$P(r,\theta,z,T) = P_m + (P_c - P_m)\left(0.5+\frac{z}{h}\right)^{n_z}\left(\frac{r-R_i}{R_o-R_i}\right)^{n_r}\left(\frac{\theta}{\theta_m}\right)^{n_\theta} \quad (1)$$

Parameter P in the above relation represents all mechanical constants or variables in the FGM material including elastic constants, density and thermal expansion coefficients. The neutral plane in the functionally graded plate structure does coincide with the geometrical mid-plane.

2.2 Mathematical modeling

2.2.1 The nonlocal strain gradient theory

Due to existence of nano-structure particles and nano-scale of the annular sector plate, integration of the scale effects in the constitutive equations is inevitable. Therefore, a convenient elasticity scheme should be used to capture the small-scale effects. In this regard, nonlocal strain gradient theory which is proven to be a powerful theory in dealing with both nano- and micro-scale structural elements is adopted in the present study. The general three-dimensional relations of this theory is as follows (Lim *et al*. 2015):

$$\sigma_{ij} - \mu^2\sigma_{ij,mm} = C_{ijkl}\left(\varepsilon_{kl} - l^2\varepsilon_{kl,mm}\right) \quad (2)$$

In the above equations, the tensor components of σ_{ij} and ε_{ij} represented the conventional stress and strains in the linear elasticity theory. However, in the NSGT they are not related to each other with a simple linear transformation. This relation also includes two more parameter and one Laplacian operator. The first parameter, μ, is called the nonlocal parameter which is directly related to the intrinsic internal material scale. The second one l, commonly called gradient length scale parameter, is the parameter incorporating the gradient of the strain tensors into calculation of stresses. It could be noticed that this theory is indeed a combination of nonlocal elasticity and strain gradient theory. Therefore, equating gradient length scale parameter and nonlocal parameter results in nonlocal elasticity and strain gradient theory, respectively:

$$(1-\mu^2\nabla^2)\sigma_{ij} = t_{ij},$$
$$\sigma_{ij} = C_{ijkl}\left(\varepsilon_{ij} - l^2\varepsilon_{ij,mm}\right). \quad (3)$$

in the above equations, the repeated indices indicates Laplacian operator with definition of $\nabla^2 = \frac{1}{r}\frac{\partial}{\partial r} + \frac{\partial^2}{\partial r^2} + \frac{1}{r^2}\frac{\partial^2}{\partial\theta^2}$.

2.2.2 Displacement field

One of the most important steps in dealing with structural members is the assumptions made for approximating displacement field. In the present study, a novel four-variable refined quasi-3D sinusoidal shear deformation theory (RQ-3DSSDT) with incorporation thickness change during deformation is considered (Thai and Kim 2013):

$$u_c(r,\theta,z,t) = u_{0c}(r,\theta,t) - z\frac{\partial w_{0c}(r,\theta,t)}{\partial r} + f(z)\frac{\partial w_{1c}(r,\theta,t)}{\partial r},$$

$$v_c(r,\theta,z,t) = v_{0c}(r,\theta,t) - z\frac{\partial w_{0c}(r,\theta,t)}{r\partial\theta} + f(z)\frac{\partial w_{1c}(r,\theta,t)}{r\partial\theta}, \quad (4)$$

$$w_c(r,\theta,z,t) = w_{0c}(r,\theta,t) + g(z)w_{1c}(r,\theta,t),$$

in the above equations $f(z) = 5h\tan^{-1}\left(\frac{z}{h}\right) - 4z$, and $g(z) = f'(z)$, respectively. For the piezoelectric layer a simpler displacement field is adopted since the thickness of the piezoelectric layers is less that the main structure in general (Reddy 2003):

$$u_p(r,\theta,z,t) = -z\frac{\partial w_{0p}(r,\theta,t)}{\partial r},$$

$$v_p(r,\theta,z,t) = -z\frac{\partial w_{0p}(r,\theta,t)}{r\partial\theta}, \quad (5)$$

$$w_p(r,\theta,z,t) = w_{0p}(r,\theta,t).$$

2.2.3 Compatibility conditions

The state of the bonding in the interface layers is another matter of concerns. For the sake of simplicity, a perfect bonding is assumed in all interface layers between piezoelectric and core layer resulting in the following relations:

$$u_p\left(r,\theta,\frac{h_c}{2},t\right) = u_c\left(r,\theta,\frac{h_c}{2},t\right),$$

$$v_p\left(r,\theta,\frac{h_c}{2},t\right) = v_c\left(r,\theta,\frac{h_c}{2},t\right), \quad (6)$$

$$w_p\left(r,\theta,\frac{h_c}{2},t\right) = w_c\left(r,\theta,\frac{h_c}{2},t\right),$$

Therefore displacement components turns into following forms using Eqs. (4)-(6):

$$u_c(r,\theta,z,t) = u_{0c}(r,\theta,t) - z\frac{\partial w_{0c}(r,\theta,t)}{\partial r} + f(z)\frac{\partial w_{1c}(r,\theta,t)}{\partial r},$$

$$v_c(r,\theta,z,t) = v_{0c}(r,\theta,t) - z\frac{\partial w_{0c}(r,\theta,t)}{r\partial\theta} + f(z)\frac{\partial w_{1c}(r,\theta,t)}{r\partial\theta},$$

$$w_c(r,\theta,z,t) = w_{0c}(r,\theta,t) + g(z)w_{1c}(r,\theta,t), \quad (7)$$

$$u_p(r,\theta,z,t) = -z\frac{\partial w_{0c}(r,\theta,t)}{\partial r} - zg\left(\frac{h_c}{2}\right)\frac{\partial w_{1c}(r,\theta,t)}{\partial r},$$

$$v_p(r,\theta,z,t) = -z\frac{\partial w_{0c}(r,\theta,t)}{r\partial\theta} - zg\left(\frac{h_c}{2}\right)\frac{\partial w_{1c}(r,\theta,t)}{r\partial\theta},$$

$$w_p(r,\theta,z,t) = w_{0c}(r,\theta,t) + g(z)w_{1c}(r,\theta,t),$$

It is a simple substitution to derive the Green's strain in small-deformation framework:

$$\varepsilon_{rr} = \frac{\partial u}{\partial r}, \varepsilon_{\theta\theta} = \frac{1}{r}\left(u + \frac{\partial v}{\partial\theta}\right), \varepsilon_{zz} = \frac{\partial w}{\partial z}, \gamma_{rz} = \frac{\partial u}{\partial z} + \frac{\partial w}{\partial r},$$
$$\gamma_{r\theta} = \frac{1}{r}\frac{\partial u}{\partial\theta} + \frac{\partial v}{\partial r} - \frac{v}{r}, \gamma_{\theta z} = \frac{\partial v}{\partial z} + \frac{1}{r}\frac{\partial w}{\partial\theta}. \quad (8)$$

Which turns into the following relations:

$$\begin{Bmatrix}\varepsilon_{rr}\\ \varepsilon_{\theta\theta}\\ \varepsilon_{zz}\\ \gamma_{\theta z}\\ \gamma_{rz}\\ \gamma_{r\theta}\end{Bmatrix} = \begin{Bmatrix}\wp_{rr}^{(0)}\\ \wp_{\theta\theta}^{(0)}\\ \wp_{zz}^{(0)}\\ \wp_{\theta z}^{(0)}\\ \wp_{rz}^{(0)}\\ \wp_{r\theta}^{(0)}\end{Bmatrix} + z\begin{Bmatrix}\wp_{rr}^{(1)}\\ \wp_{\theta\theta}^{(1)}\\ \wp_{zz}^{(1)}\\ \wp_{\theta z}^{(1)}\\ \wp_{rz}^{(1)}\\ \wp_{r\theta}^{(1)}\end{Bmatrix} + f(z)\begin{Bmatrix}\wp_{rr}^{(2)}\\ \wp_{\theta\theta}^{(2)}\\ \wp_{zz}^{(2)}\\ \wp_{\theta z}^{(2)}\\ \wp_{rz}^{(2)}\\ \wp_{r\theta}^{(2)}\end{Bmatrix} + g(z)\begin{Bmatrix}\wp_{rr}^{(3)}\\ \wp_{\theta\theta}^{(3)}\\ \wp_{zz}^{(3)}\\ \wp_{\theta z}^{(3)}\\ \wp_{rz}^{(3)}\\ \wp_{r\theta}^{(3)}\end{Bmatrix} + H(z)\begin{Bmatrix}\wp_{rr}^{(4)}\\ \wp_{\theta\theta}^{(4)}\\ \wp_{zz}^{(4)}\\ \wp_{\theta z}^{(4)}\\ \wp_{rz}^{(4)}\\ \wp_{r\theta}^{(4)}\end{Bmatrix}, \quad (9a)$$

$$\begin{Bmatrix}\varepsilon_{rrp}\\ \varepsilon_{\theta\theta p}\\ \varepsilon_{zzp}\\ \gamma_{\theta zp}\\ \gamma_{rzp}\\ \gamma_{r\theta p}\end{Bmatrix} = \begin{Bmatrix}\wp_{rrp}^{(0)}\\ \wp_{\theta\theta p}^{(0)}\\ \wp_{zzp}^{(0)}\\ \wp_{\theta zp}^{(0)}\\ \wp_{rzp}^{(0)}\\ \wp_{r\theta p}^{(0)}\end{Bmatrix} + z\begin{Bmatrix}\wp_{rrp}^{(1)}\\ \wp_{\theta\theta p}^{(1)}\\ \wp_{zzp}^{(1)}\\ \wp_{\theta zp}^{(1)}\\ \wp_{rzp}^{(1)}\\ \wp_{r\theta p}^{(1)}\end{Bmatrix}, \quad (9b)$$

In the above relations the function $H(z)$ is defined as $H(z) = \frac{\partial g(z)}{\partial z}$. Also, we have:

$$\wp_{rrc}^{(0)} = \frac{\partial u_{0c}}{\partial r}, \wp_{rrc}^{(1)} = -\frac{\partial^2 w_{0c}}{\partial r^2}, \wp_{rrc}^{(2)} = \frac{\partial^2 w_{1c}}{\partial r^2}, \wp_{rrc}^{(3)} = 0, \wp_{rrc}^{(4)} = 0, \wp_{\theta\theta c}^{(0)} = \frac{1}{r}\left(u_{0c} + \frac{\partial v_{0c}}{\partial\theta}\right), \quad (10a)$$

$$\wp_{\theta\theta c}^{(1)} = -\frac{1}{r}\left(\frac{\partial w_{0c}}{\partial r} + \frac{1}{r}\frac{\partial^2 w_{0c}}{\partial\theta^2}\right), \wp_{\theta\theta c}^{(2)} = \frac{1}{r}\left(\frac{\partial w_{1c}}{\partial r} + \frac{1}{r}\frac{\partial^2 w_{1c}}{\partial\theta^2}\right), \wp_{\theta\theta c}^{(3)} = 0, \wp_{\theta\theta c}^{(4)} = 0, \quad (10b)$$

$$\wp_{zzc}^{(0)} = 0, \wp_{zzc}^{(1)} = 0, \wp_{zzc}^{(2)} = 0, \wp_{zzc}^{(3)} = 0, \wp_{zzc}^{(4)} = H(z), \wp_{rzc}^{(0)} = 0, \wp_{rzc}^{(1)} = 0, \wp_{rzc}^{(2)} = 0, \quad (10c)$$

$$\wp_{rzc}^{(3)} = 2\frac{\partial w_{1c}}{\partial r}, \wp_{rzc}^{(4)} = 0, \wp_{r\theta c}^{(0)} = \frac{1}{r}\frac{\partial u_{0c}}{\partial\theta} + \frac{\partial v_{0c}}{\partial r} - \frac{v_{0c}}{r}, \wp_{r\theta c}^{(1)} = -\frac{2z}{r}\frac{\partial^2 w_{0c}}{\partial r\partial\theta} + \frac{2z}{r^2}\frac{\partial w_{0c}}{\partial\theta}, \quad (10d)$$

$$\wp_{r\theta c}^{(2)} = \frac{2f(z)}{r}\frac{\partial^2 w_{1c}}{\partial r\partial\theta} - \frac{2f(z)}{r^2}\frac{\partial w_{1c}}{\partial\theta}, \wp_{r\theta c}^{(3)} = 0, \wp_{r\theta c}^{(4)} = 0, \wp_{\theta zc}^{(0)} = 0, \wp_{\theta zc}^{(1)} = 0, \wp_{\theta zc}^{(2)} = 0, \quad (10e)$$

$$\wp_{\theta zc}^{(3)} = 2\frac{\partial w_{1c}}{r\partial\theta}, \wp_{\theta zc}^{(4)} = 0, \quad (10f)$$

$$\wp_{rrp}^{(0)}=0,\wp_{rrp}^{(1)}=-\frac{\partial^2 w_{bc}}{\partial r^2}-g\left(\frac{h_c}{2}\right)\frac{\partial^2 w_{sc}}{\partial r^2}, \quad (10g)$$

$$\wp_{\theta\theta p}^{(0)}=0,\wp_{\theta\theta p}^{(1)}=\frac{1}{r}\left(-\frac{\partial w_{bc}}{\partial r}-g\left(\frac{h_c}{2}\right)\frac{\partial w_{sc}}{\partial r}-\frac{1}{r}\frac{\partial^2 w_{bc}}{\partial\theta^2}-\frac{g\left(\frac{h_c}{2}\right)}{r}\frac{\partial^2 w_{sc}}{\partial\theta^2}\right), \quad (10h)$$

$$\wp_{zzp}^{(0)}=0,\wp_{zzp}^{(1)}=0,\ ,\ \wp_{\theta zp}^{(0)}=0,\wp_{\theta zp}^{(1)}=0,\ ,\ \wp_{rzp}^{(0)}=0,\wp_{rzp}^{(1)}=0\ , \quad (10i)$$

$$\wp_{r\theta p}^{(0)}=0,\wp_{r\theta p}^{(1)}=-\frac{2}{r}\frac{\partial^2 w_{bc}}{\partial r\partial\theta}-\frac{2}{r}g\left(\frac{h_c}{2}\right)\frac{\partial^2 w_{sc}}{\partial r\partial\theta}+\frac{2}{r^2}\frac{\partial w_{bc}}{\partial\theta}+\frac{2}{r^2}g\left(\frac{h_c}{2}\right)\frac{\partial w_{sc}}{\partial\theta}. \quad (10j)$$

Incorporating poroelasticity relations, the below equation is obtained for the case of the core material in NSGT:

$$\begin{aligned}(1-\mu^2\nabla^2)\sigma_{rrc}&=(1-l^2\nabla^2)\big(Q_{11c}\varepsilon_{rrc}+Q_{12c}\varepsilon_{\theta\theta c}+Q_{13c}\varepsilon_{zzc}-\gamma P_p\big),\\(1-\mu^2\nabla^2)\sigma_{\theta\theta c}&=(1-l^2\nabla^2)\big(Q_{12c}\varepsilon_{rrc}+Q_{22c}\varepsilon_{\theta\theta c}+Q_{23c}\varepsilon_{zzc}-\gamma P_p\big),\\(1-\mu^2\nabla^2)\sigma_{zzc}&=(1-l^2\nabla^2)\big(Q_{13c}\varepsilon_{rrc}+Q_{23c}\varepsilon_{\theta\theta c}+Q_{33c}\varepsilon_{zzc}-\gamma P_p\big),\\(1-\mu^2\nabla^2)\tau_{\theta zc}&=(1-l^2\nabla^2)Q_{44c}\gamma_{\theta zc},\\(1-\mu^2\nabla^2)\tau_{rzc}&=(1-l^2\nabla^2)Q_{55c}\gamma_{rzc},\\(1-\mu^2\nabla^2)\tau_{r\theta c}&=(1-l^2\nabla^2)Q_{66c}\gamma_{r\theta c},\end{aligned} \quad (11)$$

where

$$Q_{11c}=\frac{E_c(r,\theta,z)\big(1-\nu_c(r,\theta,z)\big)}{\big(1+\nu_c(r,\theta,z)\big)\big(1-2\nu_c(r,\theta,z)\big)},\quad Q_{33c}=Q_{22c}=Q_{11c},$$

$$Q_{12c}=\frac{E_c(r,\theta,z)\nu_c(r,\theta,z)}{\big(1+\nu_c(r,\theta,z)\big)\big(1-2\nu_c(r,\theta,z)\big)},\quad Q_{13c}=Q_{23c}=Q_{12c}, \quad (12)$$

$$Q_{44c}=\frac{E_c(r,\theta,z)}{2\left(1+\nu_c(r,\theta,z)\right)},Q_{66c}=Q_{55c}=Q_{44c}.$$

The other parameter in Eq. (11) can be written as follows (Liu *et al*. 2022)

$$P_p=\frac{\psi-(\varepsilon_{rr}+\varepsilon_{\theta\theta}+\varepsilon_{zz})}{\left(K^P\right)^{-1}}, \quad (13a)$$

$$K^P=-(k_t-k_u)\gamma^{-2}, \quad (13b)$$

$$k_u=\left[1-\frac{k_f\gamma^2}{(\phi-\gamma)(1-\gamma)k_f+k_f\phi}\right]k_t, \quad (13c)$$

In Eq. (13a), ψ = 0 for un-drained conditions of fluid leads to:

$$P_p=-K^P\gamma\varepsilon=-K^P(\varepsilon_{rr}+\varepsilon_{\theta\theta}+\varepsilon_{zz})\gamma \quad (14)$$

The substitution of Eq. (14) into Eq. (11) gives

$$\begin{aligned}(1-\mu^2\nabla^2)\sigma_{rrc}&=(1-l^2\nabla^2)(\bar{Q}_{11c}\varepsilon_{rrc}+\bar{Q}_{12}\varepsilon_{\theta\theta c}+\bar{Q}_{13}\varepsilon_{zzc}),\\(1-\mu^2\nabla^2)\sigma_{\theta\theta c}&=(1-l^2\nabla^2)(\bar{Q}_{12c}\varepsilon_{rrc}+\bar{Q}_{22c}\varepsilon_{\theta\theta c}+\bar{Q}_{23c}\varepsilon_{zzc}),\\(1-\mu^2\nabla^2)\sigma_{zzc}&=(1-l^2\nabla^2)(\bar{Q}_{13c}\varepsilon_{rrc}+\bar{Q}_{23c}\varepsilon_{\theta\theta c}+\bar{Q}_{33c}\varepsilon_{zzc}),\\(1-\mu^2\nabla^2)\tau_{\theta zc}&=(1-l^2\nabla^2)\bar{Q}_{44c}\gamma_{\theta zc},\\(1-\mu^2\nabla^2)\tau_{rzc}&=(1-l^2\nabla^2)\bar{Q}_{55c}\gamma_{rzc},\\(1-\mu^2\nabla^2)\tau_{r\theta c}&=(1-l^2\nabla^2)\bar{Q}_{66c}\gamma_{r\theta},\end{aligned} \quad (15)$$

where

$$\bar{Q}_{ijc}=Q_{ijc}+K\gamma^2 i,j=1,2,3.\qquad \bar{Q}_{ijc}=Q_{ijc}i=j=4,5,6. \quad (16)$$

The constitutive relations for the piezoelectric layers are developed as:

$$\begin{aligned}(1-\mu^2\nabla^2)\sigma_{rrp}&=(1-l^2\nabla^2)\big(Q_{11p}\varepsilon_{rrp}+Q_{12p}\varepsilon_{\theta\theta p}-e_{31p}E_z\big),\\(1-\mu^2\nabla^2)\sigma_{\theta\theta p}&=(1-l^2\nabla^2)\big(Q_{12p}\varepsilon_{rrp}+Q_{22p}\varepsilon_{\theta\theta p}-e_{32p}E_z\big),\\(1-\mu^2\nabla^2)\tau_{\theta zp}&=(1-l^2\nabla^2)\big(Q_{44p}\gamma_{\theta zp}-e_{24p}E_\theta\big),\\(1-\mu^2\nabla^2)\tau_{rzp}&=(1-l^2\nabla^2)\big(Q_{55p}\gamma_{rzp}-e_{15p}E_r\big),\\(1-\mu^2\nabla^2)\tau_{r\theta p}&=(1-l^2\nabla^2)\big(Q_{66p}\gamma_{r\theta p}\big),\end{aligned} \quad (17)$$

The electric displacement relations are developed as

$$\begin{aligned}(1-\mu^2\nabla^2)D_{rp}&=(1-l^2\nabla^2)\big(e_{15p}\gamma_{rzp}+\eta_{11p}E_r\big),\\(1-\mu^2\nabla^2)D_{\theta p}&=(1-l^2\nabla^2)\big(e_{15p}\gamma_{\theta zp}+\eta_{22p}E_\theta\big),\\(1-\mu^2\nabla^2)D_{zp}&=(1-l^2\nabla^2)\big(e_{31p}\varepsilon_{rrp}+e_{32p}\varepsilon_{\theta\theta p}+\eta_{33p}E_z\big),\end{aligned} \quad (18)$$

where (Gholami and Ansari 2017)

$$Q_{11p}=Q_{11}-\frac{Q_{13}^2}{Q_{33}},\ Q_{12p}=Q_{12}-\frac{Q_{13}Q_{23}}{Q_{33}},\ Q_{22p}=Q_{22}-\frac{Q_{23}^2}{Q_{33}},\quad Q_{44p}=Q_{44},\ Q_{55p}=Q_{55},\ Q_{66p}=Q_{66}, \quad (19)$$

$$e_{31p}=e_{31}-\frac{Q_{13}e_{33}}{Q_{33}},\quad e_{32p}=e_{32}-\frac{Q_{23}e_{33}}{Q_{33}},\ e_{15p}=$$

$$e_{15},\ e_{24p} = e_{24},$$

$$\eta_{11p} = \eta_{11},\ \eta_{22p} = \eta_{22},\ \eta_{33p} = \eta_{33} + \frac{e_{33}^2}{Q_{33}},$$

Electric field strength components E_r, E , E_z could be related to an electric field potential ψ as follows:

$$E_r = -\frac{\partial\psi}{\partial r},\ E_y = -\frac{1}{r}\frac{\partial\psi}{\partial\theta},\ E_z = -\frac{\partial\psi}{\partial z} \tag{20}$$

There are many forms of the electric field potential suggested in literature. In the current work, we adopted the potential function presented by Ke and Wang (2014) as given below:

$$\psi(r,\theta,z,t) = -cos(\beta z)\,\phi(r,\theta,t) + \frac{2z\phi_0}{h} \tag{21}$$

The parameter β is $\beta = \pi/h$ and ϕ_0 represents for the initial external electric. Moreover, $\phi(r,\theta,t)$ indicates variation of electric potential ϕ in the r and directions during time.

2.3 Minimum total potential energy

The powerful method of minimizing potential energy is utilized to derive equations of motion of the annular MD-FGM plate structure (Chen *et al*. 2017):

$$\delta\big((\Pi_T + \Pi_w)\text{-}\Pi_e\big)=0 \tag{22}$$

The energy term in the above relation are expressed as below:

$$\begin{gathered}\Pi_e = \int\{\sigma_{rrc}\varepsilon_{rrc} + \sigma_{\theta\theta c}\varepsilon_{\theta\theta c} + \sigma_{zzc}\varepsilon_{zzc} + \\ \tau_{rzc}\gamma_{rzc} + \tau_{\theta zc}\gamma_{\theta zc} + \tau_{r\theta c}\gamma_{r\theta c}\}dV + \int\big(\sigma_{rrp}\varepsilon_{rrp} + \\ \sigma_{\theta\theta p}\varepsilon_{\theta\theta p} + \sigma_{zzp}\varepsilon_{zzp} + \tau_{\theta zp}\gamma_{\theta zp} + \tau_{rzp}\gamma_{rzp} + \\ \tau_{r\theta p}\gamma_{r\theta p} - D_{rp}E_{rp} - D_{\theta p}E_{\theta p} - D_{zp}E_{zp}\big)dV,\end{gathered} \tag{23q}$$

$$\Pi_T = \frac{1}{2}\int\left\{\frac{N_T}{r}\frac{\partial}{\partial r}\left(r\frac{\partial w_{0c}}{\partial r}\right) + \frac{N_T}{r^2}\frac{\partial^2 w_{0c}}{\partial\theta^2}\right\}w_{0c}dA. \tag{23b}$$

The variation the external electric energy is:

$$\Pi_w = \frac{1}{2}\int N_p\left(\frac{1}{r}\frac{\partial}{\partial r}\left(r\frac{\partial w_{0c}}{\partial r}\right) + \frac{1}{r^2}\frac{\partial^2 w_{0c}}{\partial\theta^2}\right)w_{0c}dA \tag{24}$$

The term N_p electric load could be expressed as (Safarpour *et al*. 2019):

$$N_P = -2\left(e_{31} - \frac{Q_{13}e_{33}}{Q_{33}}\right)\phi_0 \tag{25}$$

Substituting Eqs. (23a-b) and (24) into Eq. (22), the following equations is obtained:

$$\delta u_{0c}\colon \frac{1}{r}\frac{\partial(rN_{rrc})}{\partial r} - \frac{N_{\theta\theta c}}{r} + \frac{\partial N_{r\theta c}}{r\partial\theta} = 0, \tag{26a}$$

$$\delta v_{0c}\colon \frac{1}{r}\frac{\partial N_{\theta\theta c}}{\partial\theta} + \frac{1}{r}\frac{\partial(rN_{r\theta c})}{\partial r} + \frac{N_{r\theta c}}{r} = 0, \tag{26b}$$

$$\begin{gathered}\delta w_{0c}\colon \frac{1}{r}\frac{\partial^2(rM_{rrc})}{\partial r^2} - \frac{1}{r}\frac{\partial M_{\theta\theta c}}{\partial r} + \frac{1}{r^2}\frac{\partial^2 M_{\theta\theta c}}{\partial\theta^2} + \\ \frac{2}{r}\frac{\partial^2 M_{r\theta c}}{\partial r\partial\theta} + \frac{2}{r^2}\frac{\partial M_{r\theta c}}{\partial\theta} + \frac{1}{r}\frac{\partial^2(rM_{rrp})}{\partial r^2} - \frac{1}{r}\frac{\partial M_{\theta\theta p}}{\partial r} + \\ \frac{1}{r^2}\frac{\partial^2 M_{\theta\theta p}}{\partial\theta^2} + \frac{2}{r}\frac{\partial^2 M_{r\theta p}}{\partial r\partial\theta} + \frac{2}{r^2}\frac{\partial M_{r\theta p}}{\partial\theta} - N_p\nabla^2 w_{0c} = \\ N_T\nabla^2 w_{0c},\end{gathered} \tag{26c}$$

$$\begin{gathered}\delta w_{1c}\colon -\frac{1}{r}\frac{\partial^2(rP_{rrc})}{\partial r^2} + \frac{1}{r}\frac{\partial P_{\theta\theta c}}{\partial r} - \frac{1}{r^2}\frac{\partial^2 P_{\theta\theta c}}{\partial\theta^2} - R_{zzc} + \\ \frac{2}{r}\frac{\partial(rQ_{rzc})}{\partial r} + \frac{2}{r}\frac{\partial Q_{\theta zc}}{\partial\theta} - \frac{2}{r}\frac{\partial^2 P_{r\theta c}}{\partial r\partial\theta} - \frac{2}{r^2}\frac{\partial P_{r\theta c}}{\partial\theta} + \\ \frac{g\left(\frac{h_c}{2}\right)}{r}\frac{\partial^2(rM_{rrp})}{\partial r^2} - \frac{g\left(\frac{h_c}{2}\right)}{r}\frac{\partial M_{\theta\theta p}}{\partial r} + \frac{g\left(\frac{h_c}{2}\right)}{r^2}\frac{\partial^2 M_{\theta\theta p}}{\partial\theta^2} + \\ \frac{2g\left(\frac{h_c}{2}\right)}{r}\frac{\partial^2 M_{r\theta p}}{\partial r\partial\theta} + \frac{2g\left(\frac{h_c}{2}\right)}{r^2}\frac{\partial M_{r\theta p}}{\partial\theta} = 0,\end{gathered} \tag{26d}$$

$$\begin{gathered}\delta\phi\colon \int_V\left\{\frac{1}{r}\frac{\partial(rD_r)}{\partial r}cos(\beta z) + \frac{\partial D_\theta}{r\partial\theta}cos(\beta z) + \right. \\ \left.\beta D_z\,sin(\beta z)\right\}dV = 0,\end{gathered} \tag{26e}$$

The natural boundary conditions are given as:

$$\delta u_{0c} = 0 \quad \text{or} \quad (N_{rrc})\hat{n}_r + \left(\frac{N_{r\theta c}}{r}\right)\hat{n}_\theta = 0, \tag{27a}$$

$$\delta v_{0c} = 0 \quad \text{or} \quad (N_{r\theta c})\hat{n}_r + \left(\frac{N_{\theta\theta c}}{r}\right)\hat{n}_\theta = 0, \tag{27b}$$

$$\begin{gathered}\delta w_{0c} = 0 \quad \text{or} \left\{\frac{\partial(rM_{rrc})}{r\partial r} - \frac{M_{\theta\theta c}}{r} + 2\frac{\partial M_{r\theta c}}{r\partial\theta} + \right. \\ \left.\frac{\partial(rM_{rrp})}{r\partial r} - \frac{M_{\theta\theta p}}{r} + \frac{\partial M_{r\theta p}}{r\partial\theta}\right\}\hat{n}_r + \left\{\frac{\partial M_{\theta\theta c}}{r^2\partial\theta} + \frac{M_{r\theta c}}{r^2} - \right. \\ \left.\frac{\partial M_{r\theta c}}{r^2\partial\theta} + \frac{\partial M_{\theta\theta p}}{r^2\partial\theta} + \frac{\partial M_{r\theta p}}{r\partial r} + \frac{2M_{r\theta p}}{r^2}\right\}\hat{n}_\theta = 0\,,\end{gathered} \tag{27c}$$

$$\begin{gathered}\delta w_{1c} = 0 \ \text{or} \left(\frac{\partial(rP_{rrc})}{r\partial r} - \frac{P_{\theta\theta c}}{r} - 2N_{rzc} + \frac{\partial P_{r\theta c}}{r\partial\theta} + \right. \\ g\left(\frac{h_c}{2}\right)\frac{\partial(rM_{rrp})}{r\partial r} - g\left(\frac{h_c}{2}\right)\frac{M_{\theta\theta p}}{r} + g\left(\frac{h_c}{2}\right)\frac{\partial M_{r\theta p}}{r\partial\theta}\Big)\hat{n}_r + \\ \left(\frac{\partial P_{\theta\theta c}}{r^2\partial\theta} - \frac{2}{r}N_{\theta zc} + \frac{2P_{r\theta c}}{r^2} + \frac{\partial P_{r\theta c}}{r\partial r} + g\left(\frac{h_c}{2}\right)\frac{\partial M_{\theta\theta p}}{r^2\partial\theta} + \right. \\ \left.g\left(\frac{h_c}{2}\right)\frac{\partial M_{r\theta p}}{r\partial r} + g\left(\frac{h_c}{2}\right)\frac{2M_{r\theta p}}{r^2}\right)\hat{n}_\theta = 0\,,\end{gathered} \tag{27d}$$

$$\frac{\partial\delta w_{0c}}{\partial r} = 0 \quad \text{or} \quad \left(M_{rrc} + M_{rrp}\right)\hat{n}_r + \left(\frac{M_{r\theta c}}{r} + \frac{M_{r\theta p}}{r}\right)\hat{n}_\theta = 0, \tag{27e}$$

$$\frac{\partial\delta w_{0c}}{\partial\theta} = 0 \quad \text{or} \quad \left(\frac{M_{r\theta c}}{r} + \frac{M_{r\theta p}}{r}\right)\hat{n}_r + \left(\frac{M_{\theta\theta c}}{r^2} + \frac{M_{\theta\theta p}}{r^2}\right)\hat{n}_\theta = 0, \tag{27f}$$

$$\frac{\partial\delta w_{1c}}{\partial r} = 0 \quad \text{or} \quad \left(P_{rrc} + g\left(\frac{h_c}{2}\right)M_{rrp}\right)\hat{n}_r + \left(\frac{P_{r\theta c}}{r} + g\left(\frac{h_c}{2}\right)\frac{M_{r\theta p}}{r}\right)\hat{n}_\theta = 0, \tag{27g}$$

$$\frac{\partial\delta w_{1c}}{\partial\theta} = 0 \quad \text{or} \quad \left(\frac{P_{r\theta c}}{r} + g\left(\frac{h_c}{2}\right)\frac{M_{r\theta p}}{r}\right)\hat{n}_r + \left(\frac{P_{\theta\theta c}}{r^2} + g\left(\frac{h_c}{2}\right)\frac{M_{\theta\theta p}}{r^2}\right)\hat{n}_\theta = 0, \tag{27h}$$

$$\delta\phi = 0. \tag{27i}$$

where

$$\begin{Bmatrix}N_{rrc}\\ M_{rrc}\\ P_{rrc}\\ Q_{rrc}\\ R_{rrc}\end{Bmatrix} = \int_V\begin{Bmatrix}\sigma_{rrc}\\ z\times\sigma_{rrc}\\ f(z)\times\sigma_{rrc}\\ g(z)\times\sigma_{rrc}\\ H(z)\times\sigma_{rrc}\end{Bmatrix}rdrd\theta dz, \tag{28}$$

$$\begin{Bmatrix} N_{\theta\theta c} \\ M_{\theta\theta c} \\ P_{\theta\theta c} \\ Q_{\theta\theta c} \\ R_{\theta\theta c} \end{Bmatrix} = \int_V \begin{Bmatrix} \sigma_{\theta\theta c} \\ z \times \sigma_{\theta\theta c} \\ f(z) \times \sigma_{\theta\theta c} \\ g(z) \times \sigma_{\theta\theta c} \\ H(z) \times \sigma_{\theta\theta c} \end{Bmatrix} r dr d\theta dz,$$

$$\begin{Bmatrix} N_{zzc} \\ M_{zzc} \\ P_{zzc} \\ Q_{zzc} \\ R_{zzc} \end{Bmatrix} = \int_V \begin{Bmatrix} \sigma_{zzc} \\ z \times \sigma_{zzc} \\ f(z) \times \sigma_{zzc} \\ g(z) \times \sigma_{zzc} \\ H(z) \times \sigma_{zzc} \end{Bmatrix} r dr d\theta dz,$$

$$\begin{Bmatrix} N_{\theta zc} \\ M_{\theta zc} \\ P_{\theta zc} \\ Q_{\theta zc} \\ R_{\theta zc} \end{Bmatrix} = \int_V \begin{Bmatrix} \tau_{\theta zc} \\ z \times \tau_{\theta zc} \\ f(z) \times \tau_{\theta zc} \\ g(z) \times \tau_{\theta zc} \\ H(z) \times \tau_{\theta zc} \end{Bmatrix} r dr d\theta dz,$$

$$\begin{Bmatrix} N_{rzc} \\ M_{rzc} \\ P_{rzc} \\ Q_{rzc} \\ R_{rzc} \end{Bmatrix} = \int_V \begin{Bmatrix} \tau_{rzc} \\ z \times \tau_{rzc} \\ f(z) \times \tau_{rzc} \\ g(z) \times \tau_{rzc} \\ H(z) \times \tau_{rzc} \end{Bmatrix} r dr d\theta dz,$$

$$\begin{Bmatrix} N_{r\theta c} \\ M_{r\theta c} \\ P_{r\theta c} \\ Q_{r\theta c} \\ R_{r\theta c} \end{Bmatrix} = \int_V \begin{Bmatrix} \tau_{r\theta c} \\ z \times \tau_{r\theta c} \\ f(z) \times \tau_{r\theta c} \\ g(z) \times \tau_{r\theta c} \\ H(z) \times \tau_{r\theta c} \end{Bmatrix} r dr d\theta dz,$$

$$\begin{bmatrix} N_{rrp} \\ N_{\theta\theta p} \\ N_{zzp} \end{bmatrix} = \int_V \begin{Bmatrix} \sigma_{rrp} \\ \sigma_{\theta\theta p} \\ \sigma_{zzp} \end{Bmatrix} r dr d\theta dz,$$

$$\begin{bmatrix} M_{rrp} \\ M_{\theta\theta p} \\ M_{zzp} \end{bmatrix} = \int_V \begin{Bmatrix} z \times \sigma_{rrp} \\ z \times \sigma_{\theta\theta p} \\ z \times \sigma_{zzp} \end{Bmatrix} r dr d\theta dz,$$

$$\begin{bmatrix} N_{\theta zp} \\ N_{rzp} \\ N_{r\theta p} \end{bmatrix} = \int_V \begin{Bmatrix} \tau_{\theta zp} \\ \tau_{rzp} \\ \tau_{r\theta p} \end{Bmatrix} r dr d\theta dz,$$

$$\begin{bmatrix} M_{\theta zp} \\ M_{rzp} \\ M_{r\theta p} \end{bmatrix} = \int_V \begin{Bmatrix} z \times \tau_{\theta zp} \\ z \times \tau_{rzp} \\ z \times \tau_{r\theta p} \end{Bmatrix} r dr d\theta dz,$$

Substituting Eqs. (15), (17) and (18) into Eqs. (26a-e), the governing equations of nano-scale disk made of MD-FGM could be expressed in terms of displacement components as below:

$$\delta u_{0c}: (1-\ell^2\nabla^2)\left(\frac{1}{r}\frac{\partial(rN_{rrc})}{\partial r} - \frac{N_{\theta\theta c}}{r} + \frac{\partial N_{r\theta c}}{r\partial\theta}\right) = 0, \quad (29a)$$

$$\delta v_{0c}: (1-\ell^2\nabla^2)\left(\frac{1}{r}\frac{\partial N_{\theta\theta c}}{\partial\theta} + \frac{1}{r}\frac{\partial(rN_{r\theta c})}{\partial r} + \frac{N_{r\theta c}}{r}\right) = 0, \quad (29b)$$

$$\delta w_{0c}: (1-\ell^2\nabla^2)\left(\frac{1}{r}\frac{\partial^2(rM_{rrc})}{\partial r^2} - \frac{1}{r}\frac{\partial M_{\theta\theta c}}{\partial r} + \frac{1}{r^2}\frac{\partial^2 M_{\theta\theta c}}{\partial\theta^2} + \frac{2}{r}\frac{\partial^2 M_{r\theta c}}{\partial r\partial\theta} + \frac{2}{r^2}\frac{\partial M_{r\theta c}}{\partial\theta} + \frac{1}{r}\frac{\partial^2(rM_{rrp})}{\partial r^2} - \frac{1}{r}\frac{\partial M_{\theta\theta p}}{\partial r} + \frac{1}{r^2}\frac{\partial^2 M_{\theta\theta p}}{\partial\theta^2} + \frac{2}{r}\frac{\partial^2 M_{r\theta p}}{\partial r\partial\theta} + \frac{2}{r^2}\frac{\partial M_{r\theta p}}{\partial\theta}\right) - (1-\mu^2\nabla^2)N_p\nabla^2 w_{0c} = (1-\mu^2\nabla^2)N_T\nabla^2 w_{0c},$$

$$\delta w_{1c}: (1-\ell^2\nabla^2)\left(-\frac{1}{r}\frac{\partial^2(rP_{rrc})}{\partial r^2} + \frac{1}{r}\frac{\partial P_{\theta\theta c}}{\partial r} - \frac{1}{r^2}\frac{\partial^2 P_{\theta\theta c}}{\partial\theta^2} - R_{zzc} + \frac{2}{r}\frac{\partial(rQ_{rzc})}{\partial r} + \frac{2}{r}\frac{\partial Q_{\theta zc}}{\partial\theta} - \frac{2}{r}\frac{\partial^2 P_{r\theta c}}{\partial r\partial\theta} - \frac{2}{r^2}\frac{\partial P_{r\theta c}}{\partial\theta} + \frac{g\left(\frac{h_c}{2}\right)}{r}\frac{\partial^2(rM_{rrp})}{\partial r^2} - \frac{g\left(\frac{h_c}{2}\right)}{r}\frac{\partial M_{\theta\theta p}}{\partial r} + \frac{g\left(\frac{h_c}{2}\right)}{r^2}\frac{\partial^2 M_{\theta\theta p}}{\partial\theta^2} + \frac{2g\left(\frac{h_c}{2}\right)}{r}\frac{\partial^2 M_{r\theta p}}{\partial r\partial\theta} + \frac{2g\left(\frac{h_c}{2}\right)}{r^2}\frac{\partial M_{r\theta p}}{\partial\theta}\right) = 0, \quad (29d)$$

$$\delta\phi: \int_V (1-\ell^2\nabla^2)\left\{\frac{1}{r}\frac{\partial(rD_r)}{\partial r}cos(\beta z) + \frac{\partial D_\theta}{r\partial\theta}cos(\beta z) + \beta D_z\, sin(\beta z)\right\} dV = 0, \quad (29e)$$

3. Solution procedure

As the governing equations are finalized in term of displacement components, the solution strategy is now presented. Complex equations derived in the previous section are barely possible to be solved by analytical solution except for some certain cases. Therefore, for general case of equations a reliable and efficient numerical should be employed. The discrete singular convolution (DSC) is a powerful method is solving differential equations which is presented by Wei *et al*. (2001). The essence of this method is based on the following convolution integral which is discretized in the case of solving differential equations:

$$F(t) = (T * \eta)(t) = \int_{-\infty}^{+\infty} T(t-\xi)\eta(\xi)\, d\xi, \xi = r, \theta \quad (30)$$

The kernel of the integral is chosen so that the integral form of Eq. (30) become discretized. The following form of the kernel is chesen in the present study (Wei 2001, Lim *et al*. 2005):

$$\delta_{\Delta,\chi}(\xi - \xi_k) = \frac{sin\left[\frac{\pi}{\Delta}(\xi - \xi_k)\right]}{\frac{\pi}{\Delta}(\xi - \xi_k)} e^{-\frac{(\xi-\xi_k)^2}{2\chi^2}}, \chi > 0 \quad (31)$$

The final form of the integral could be expresses as (Wei *et al*. 2001):

$$F_\alpha(t) = \sum_k T_\alpha(t - \xi_k) f(\xi_k) \quad (32)$$

In the above equaiton $F_\alpha(t)$ is an approximation to function F(t) and $\{\xi_k\}$is a chosen set of discrete grids on which the DSC of Eq. (32) is well defined (Zhao and Wei 2002). Based on this selected form the derivative of the original function could be approximated as follows:

$$\left.\frac{d^n f(\xi)}{df^n}\right|_{\xi=\xi_i} \quad (33)$$

$$= f^{(n)}(\xi) \approx \sum_{k=-M}^{M} \delta_{\Delta,\chi}^{(n)}(\xi_i - \xi_k) f(\xi_k), (n = 0,1,2,\dots.)$$

where superscript n denotes the nth-order derivative with respect to ξ. The above equation requires derivative of the selected kernel $\delta_{\Delta,\chi}^{(n)}(\xi - \xi_j)$ which could be calculated using Eq. (33) and the derivatives become (Hou *et al*. 2005):

$$\delta_{\Delta,\chi}^{(n)}(\xi - \xi_j) = \frac{d^n}{d\xi^n}\left[\delta_{\Delta,\chi}(\xi - \xi_j)\right]\Big|_{\xi=\xi_i} \quad (34)$$

In the following examples of derivative extraction is presented up to fourth-degree for a sample function f:

$$\delta_{\Delta,\chi}^{(2)}(\xi - \xi_j) = \frac{d^2}{d\xi^2}\left[\delta_{\Delta,\chi}(\xi - \xi_j)\right]\Big|_{\xi=\xi_i} \quad (35)$$

The discretized forms of Eq. (35) can then be expressed as

$$f^{(2)}(\xi) = \frac{d^2 f}{d\xi^2}\bigg|_{x=x_i} \approx \sum_{k=-M}^{M} \delta_{\Delta,\chi}^{(2)}(k\Delta\xi_N) f_{i+k,j} \quad (36)$$

For Shannon's kernel, the related derivatives is defined in Ref. (Civalek 2017).

In which $\Delta = \pi/(N-1)$ is the grid spacing and N is the number of grid points for the computational domain $\xi_0 <\dots< \xi_{N-1}$, with a total of 2M fictitious grid points, $\xi_{-M} <\dots< \xi_{-1}$ and $\xi_N <\dots< \xi_{N-1+M}$, Finally the modal equations of the structure could be compacted in the following matric form including boundary conditions:

$$\left\{\begin{bmatrix}[\mathcal{F}_{dd}] & [\mathcal{F}_{db}]\\ [\mathcal{F}_{bd}] & [\mathcal{F}_{bb}]\end{bmatrix}\Delta T_{cr} + \begin{bmatrix}[\mathcal{K}_{dd}] & [\mathcal{K}_{db}]\\ [\mathcal{K}_{bd}] & [\mathcal{K}_{bb}]\end{bmatrix}\right\}\begin{Bmatrix}\Xi_d\\ \Xi_b\end{Bmatrix} = 0 \quad (37)$$

The thermal buckling of the problem are derived as solutions of Eq. (37).

4. Presenting artificial neural networks for the mentioned problem

The development of intelligent prosthetic hands has made significant advancements in recent years, primarily through the integration of artificial neural networks (ANNs) and nanoscale technologies. This integration has opened up new avenues for enhancing the functionality, responsiveness, and adaptability of prosthetic devices, allowing individuals with limb loss to experience improved quality of life. The primary objective of optimizing intelligent prosthetic hands lies in improving their performance to closely mimic natural hand movements while providing the user with an intuitive control interface. In the context of intelligent prosthetics, performance is defined by the system's ability to interpret signals from the human nervous system, respond to complex motor commands, and adapt to the changing demands of the user's daily activities. Thus, the convergence of ANNs with nanoscale technologies offers a promising solution to the challenges faced in achieving these goals. Artificial neural networks have gained attention as a robust computational tool for interpreting bioelectric signals from muscles and nerves. These networks, inspired by the structure of the human brain, are capable of learning and adapting to different patterns of input signals. For prosthetic hands, ANNs can process electromyographic (EMG) signals, which are electrical signals generated by muscle contractions. By training the neural network on these EMG signals, it becomes possible to classify different hand movements and translate them into corresponding actions of the prosthetic hand. This real-time learning capability of ANNs significantly enhances the responsiveness and dexterity of prosthetic hands, allowing users to perform complex tasks with greater ease. Moreover, the use of deep learning techniques enables the ANN to continuously learn and refine its understanding of the user's movement patterns, improving the device's long-term performance. In parallel with the advancements in artificial neural networks, nanoscale technologies have emerged as critical enablers of high-performance prosthetic systems. Nanosensors, for instance, provide unprecedented sensitivity in detecting bioelectrical signals from nerves and muscles, ensuring that even the slightest muscle contractions are captured and processed. Furthermore, nanomaterials are being utilized to develop more flexible and lightweight prosthetic components, which contribute to user comfort and increase the prosthetic's longevity. The integration of nanotechnology with intelligent prosthetics also facilitates the development of energy-efficient devices, addressing one of the major limitations of traditional prosthetics, which require frequent battery changes. Additionally, the use of nanoscale transducers enhances the communication between the neural network and the mechanical components of the prosthetic hand, ensuring smoother and more precise control of movement. The optimization of intelligent prosthetic hands using artificial neural networks and nanoscale technologies involves a multi-faceted approach

Table 1 The temperature-dependent material properties of the MD-FGMs annular nanoplates (Reddy and Chin 1998)

Ceramic (Al_2O_3)					
P	P_0	P_{-1}	P_1	P_2	P_3
$E_c[pa]$	348.43×10^9	0	-3.070×10^{-4}	2.160×10^{-7}	-8.946×10^{-11}
$\alpha_c\left[\frac{1}{K}\right]$	5.8723×10^{-6}	0	9.095×10^{-4}	0	0
$K_c\left[\frac{W}{mK}\right]$	13.723	0	-1.032×10^{-3}	5.466×10^{-7}	-7.876×10^{-11}
v_c	0.2400	0	0	0	0
$\rho_c\left[\frac{Kg}{m^3}\right]$	2370	0	0	0	0
Metal (SUS304)					
$E_m[pa]$	201.04×10^9	0	3.079×10^{-4}	-6.534×10^{-7}	0
$\alpha_m\left[\frac{1}{K}\right]$	12.330×10^{-6}	0	8.086×10^{-4}	0	0
$K_m\left[\frac{W}{mK}\right]$	15.379	0	-1.264×10^{-3}	2.092×10^{-6}	-7.223×10^{-10}
v_m	0.3262	0	-2.002×10^{-4}	3.797×10^{-7}	0
$\rho_m\left[\frac{Kg}{m^3}\right]$	8166	0	0	0	0

Table 2 Material properties of PZT-4 (Pietrzakowski 2008)

Q_{11} *(GPa)*	Q_{22} *(GPa)*	Q_{12} *(GPa)*	Q_{13} *(GPa)*	Q_{33} *(GPa)*	Q_{44} *(GPa)*	Q_{55} *(GPa)*	Q_{66} *(GPa)*
132	132	71	73	115	26	26	30.5
e_{31} *(C/m²)*	e_{32} *(C/m²)*	e_{33} *(C/m²)*	e_{15} *(C/m²)*	e_{24} *(C/m²)*	$_{11}$ *(C/V m)*	$_{22}$ *(C/V m)*	$_{33}$ *(C/V m)*
−4.1	−4.1	14.1	10.5	10.5	5.841×10^{-9}	5.841×10^{-9}	7.124×10^{-9}
ρ *(kg/m³)*							
7500							

Table 3 Accuracy of the thermal buckling factor λ_T $[=12(1+\nu)\alpha\Delta T(a/h)^2]$ for homogeneous annular Mindlin plates under uniform temperature rise.

	$\frac{R_i}{R_o}=0.2$			$\frac{R_i}{R_o}=0.4$			$\frac{R_i}{R_o}=0.6$		
SS									
$\frac{h}{R_o}$	Ref. (Sepahi *et al*. 2011)	Ref. (Wang *et al*. 1994)	Present	Ref. (Sepahi *et al*. 2011)	Ref. (Wang *et al*. 1994)	Present	Ref. (Sepahi *et al*. 2011)	Ref. (Wang *et al*. 1994)	Present
0.05	18.5471	18.5416	18.5412	28.6417	28.6332	28.6315	60.1986	60.1865	60.1561
0.1	17.7252	17.7241	17.7202	26.9211	26.9153	26.9134	53.2518	53.2462	53.2054
0.15	16.5100	16.5079	16.5085	24.4721	24.4629	24.4611	44.6630	44.6624	44.6184
0.2	15.0695	15.0699	15.0675	21.7093	21.7062	21.7026	36.4367	36.4332	36.4034
SC									
0.05	40.7178	40.1322	40.1124	61.1677	61.1680	61.1381	122.3041	122.1025	122.0783
0.1	37.4454	36.7599	36.7451	53.9609	53.9490	53.9289	95.9334	95.9224	95.7854
0.15	33.0228	32.2851	32.2672	45.1082	45.1046	45.0985	70.6129	70.5936	70.5012
0.2	28.3376	27.6045	27.5812	36.6890	36.5904	36.6691	51.6063	51.5236	51.5045
CS									
0.05	27.9670	27.8256	27.8098	49.9565	49.9566	49.9371	109.5716	109.4116	109.2043
0.1	25.9118	25.6137	25.6045	44.2265	44.2225	44.2045	86.1880	86.1740	86.1192
0.15	23.0852	22.7338	22.7145	37.1368	37.1246	37.1056	63.6357	63.6325	63.6054
0.2	20.0331	19.7580	19.7234	30.3496	30.3490	30.3134	46.6745	46.6625	46.6456

Table 4 Convergence study in DSCM from annular sector FG plate considering $h=0.1\,nm$, $R_i=40h$, $\theta=\frac{\pi}{4}$, $n_r,n_\theta,n_z=0.5$, $l=h$, $\mu=h$, $\emptyset_0=0.1\,(mV)$, $A_P=\frac{A_T}{4}$, and $R_o=2R_i$

Boundary conditions		(N_r,N_θ,J)					
		(15,15,2)	(20,20,2.5)	(25,25,3)	(30,30,3)	(30,30,3.5)	(35,35,3.5)
SSSS	$K^p=0$	91.6892	87.6578	87.6371	87.6371	87.6371	87.6371
	$K^p\neq0$	95.7812	91.7891	91.7781	91.7781	91.7781	91.7781
SCSC	$K^p=0$	205.9056	197.7567	197.7419	197.7419	197.7419	197.7419
	$K^p\neq0$	212.8934	206.5591	206.5430	206.5430	206.5430	206.5430
CSCS	$K^p=0$	156.9043	149.2805	149.2792	149.2792	149.2792	149.2792
	$K^p\neq0$	163.0956	156.1794	156.1631	156.1631	156.1631	156.1631
CCCC	$K^p=0$	258.9056	247.0245	247.0015	247.0015	247.0015	247.0015
	$K^p\neq0$	268.9075	257.9461	257.9312	257.9312	257.9312	257.9312

that encompasses signal processing, materials engineering, and machine learning. This optimization process focuses on improving the system's accuracy in recognizing user intent, minimizing response time, and enhancing the durability and adaptability of the prosthetic hand. Future research in this field is expected to explore more advanced neural network architectures and leverage emerging nanoscale technologies for even greater improvements in prosthetic functionality. By integrating these cutting-edge technologies, the next generation of intelligent prosthetics aims to achieve seamless

Table 5 The effect of outer to inner radii aspect ratio on the ΔT_c for different boundary condition and two scenarios for parameter K^p with $h = 0.1\,nm$, $R_i = 40h$, $\theta = \frac{\pi}{4}$, $n_r, n_\theta, n_z = 0.5$, $l = h$, $\mu = h$, $\emptyset_0 = 0.1\,(mV)$, and $A_P = \frac{A_T}{4}$

Boundary conditions		$R_o = 2R_i$	$R_o = 2.1R_i$	$R_o = 2.2R_i$	$R_o = 2.3R_i$	$R_o = 2.4R_i$	$R_o = 2.5R_i$
SSSS	$K^p = 0$	87.6371	76.0516	66.8849	59.4574	53.3188	48.1605
	$K^p \neq 0$	91.7781	79.6715	70.0910	62.3273	55.9100	50.5169
SCSC	$K^p = 0$	197.7419	163.5280	137.7122	117.7588	102.0138	89.3636
	$K^p \neq 0$	206.5430	170.8482	143.9108	123.0877	106.6545	93.4502
CSCS	$K^p = 0$	149.2792	135.9476	124.4243	114.2590	105.1923	97.0616
	$K^p \neq 0$	156.1631	142.2373	130.1984	119.5767	110.1017	101.6039
CCCC	$K^p = 0$	247.0015	214.2428	189.0689	169.1142	152.8639	139.3189
	$K^p \neq 0$	257.9312	223.7497	197.4786	176.6518	159.6898	145.5511

interaction between the user and the prosthetic hand, offering individuals with limb loss the opportunity to regain a higher degree of autonomy and perform everyday tasks with confidence. Ultimately, the synergy between ANNs and nanoscale technologies represents a transformative step toward the realization of fully optimized, high-performance prosthetic hands.

5. Results and discussion

5.1 Material properties

The functionally graded composite structure in the present study composed from different materials. The material properties of each component is presented for different P_i in Tables 1 and 2. In Table 1, the material properties of functionally graded components is presented which are ceramic Al_2O_3 and SUS304. On the other hand, the piezoelectric layer is designated by PTZ-4 with mechanical and electromechanical properties given in Table 2.

5.2 Validation

Validation process includes solving a benchmark problem using the presented methodology and comparing results with other approaches. In this regard, two references Sepahi *et al*. (2011) and Wang *et al*. (1994) are selected for comparing the natural frequencies results with the current method in obtaining the thermal buckling factor of annular plates. The outcome of the three studies are presented in Table 3. The values of the thermal buckling factor given in this table demonstrate that the current approach in solving equations of composite structures under thermal loading is reliable and could be utilized in further analyses.

5.3 Convergency

Another important issue to be considered in the numerical methods basing on the discretization approaches is to investigate the convergency of the results for increasing number of discretized regions. In doing so, for the case of an annular sector plate with four different boundary conditions, thermal buckling factor are obtained and given in Table 4. It could be observed from the values of this table that after $(N_r, N_\theta, J) = (25,25,3)$, the values of the critical temperature increase converges. Therefore, in the following analyses the above discretization scheme will be employed. One another feature of the values given in Table 4 is the increasing value of the critical temperature change with increase in the stiffness of the structure due to change in the boundary conditions such that the fully simply-supported structure has the lowest value of the thermal change while fully clamped condition causes highest thermal change. In addition, there is a slight difference between the values of ΔT_c as result of change in K^p from zero to non-zero values.

5.4 Parametric results

In this section, influence of changing different geometrical and material parameters on the buckling behavior of the annular sector plate structure is investigated. In this regard, Table 5 presents effect of outer to inner radii aspect ratio on the ΔT_c for different boundary condition and two scenarios for parameter K^p. It is seen that increasing the values of R_o/R_i ratio results in significant decrease in the ΔT_c such that changing R_o/R_i from 2 to 2.5 approximately reduces the ΔT_c up to 45% and, hence, deteriorate the stability of the structure under thermal loadings. Effect of the boundary condition and parameter K^p is similar to those discussed above, with increase in the boundary condition stiffness the ΔT_c increases considerably.

Values presented in Table 5 are converted to graphical charts in Fig. 2 to have a better understanding on the effects of geometry aspect ratio on the critical temperature increase. Four graphs are shown in this figure for four different boundary condition. The critical temperature reduces in a near linear manner as the aspect ratio R_o/R_i increases in all boundary conditions and values of parameter K^p. On the other hand, effect of parameter K^p is similar in all the boundary and geometrical conditions.

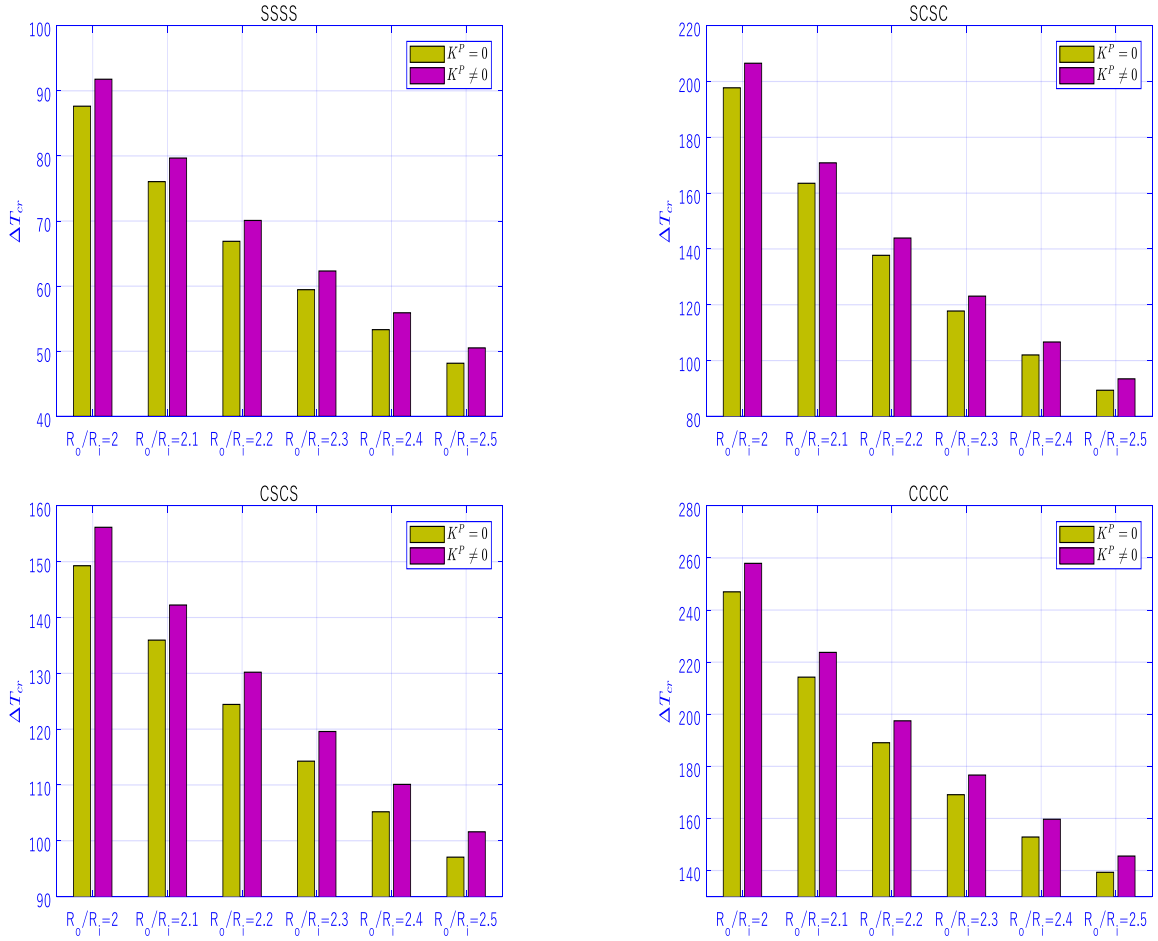

Fig. 2 Effect of geometrical aspect ratio and K^p on the critical temperature of the presented annular sector plate structure considering $h = 0.1\,nm$, $R_i = 40h$, $\theta = \frac{\pi}{4}$, $n_r, n_\theta, n_z = 0.5$, $l = h$, $\mu = h$, $\emptyset_0 = 0.1\,(mV)$, and $A_P = \frac{A_T}{4}$

Table 6 Effect of θ parameter and boundary conditions on the critical temperature of the presented annular sector plate structure considering $h = 0.1\,nm$, $R_i = 40h$, $R_o = 2R_i$, $n_r, n_\theta, n_z = 0.5$, $l = h$, $\mu = h$, $\emptyset_0 = 0.1\,(mV)$, and $A_P = \frac{A_T}{4}$

Boundary conditions		$\theta = \frac{\pi}{6}$	$\theta = \frac{\pi}{4}$	$\theta = \frac{\pi}{3}$	$\theta = \frac{\pi}{2}$	$\theta = \frac{2\pi}{3}$	$\theta = \pi$
SSSS	$K^p = 0$	133.9708	87.6371	71.8649	61.1190	57.5383	55.0613
	$K^p \neq 0$	140.2096	91.7781	75.2561	63.9715	60.2018	57.5898
SCSC	$K^p = 0$	215.3528	197.7419	200.1410	197.9602	199.3651	198.7595
	$K^p \neq 0$	225.0033	206.5430	208.9714	206.7633	208.2269	207.5836
CSCS	$K^p = 0$	291.2421	149.2792	99.1800	68.7618	60.5189	55.8527
	$K^p \neq 0$	304.3750	156.1631	103.8048	71.9692	63.3241	58.4200
CCCC	$K^p = 0$	380.2072	247.0015	216.6461	209.3456	205.0011	201.1021
	$K^p \neq 0$	396.8646	257.9312	226.2223	218.3732	214.0840	210.0334

In Fig. 3, the graphical demonstration of data in Table 6 is shown. As seen, effect of increasing span angle of the angular sector is more prominent in the low values of the span angle. With increase in the span angle, the critical temperature change continues to decrease but in lower rate compared to the low values of span angle. This behavior is common among all the boundary conditions.

5.5 Results of the presented machine learning algorithm

The current research looks at five statistical indicators, such as coefficient of determination (R^2) and root mean square error (RMSE), to assess the model's effectiveness. Here are several methods to ascertain their identity:

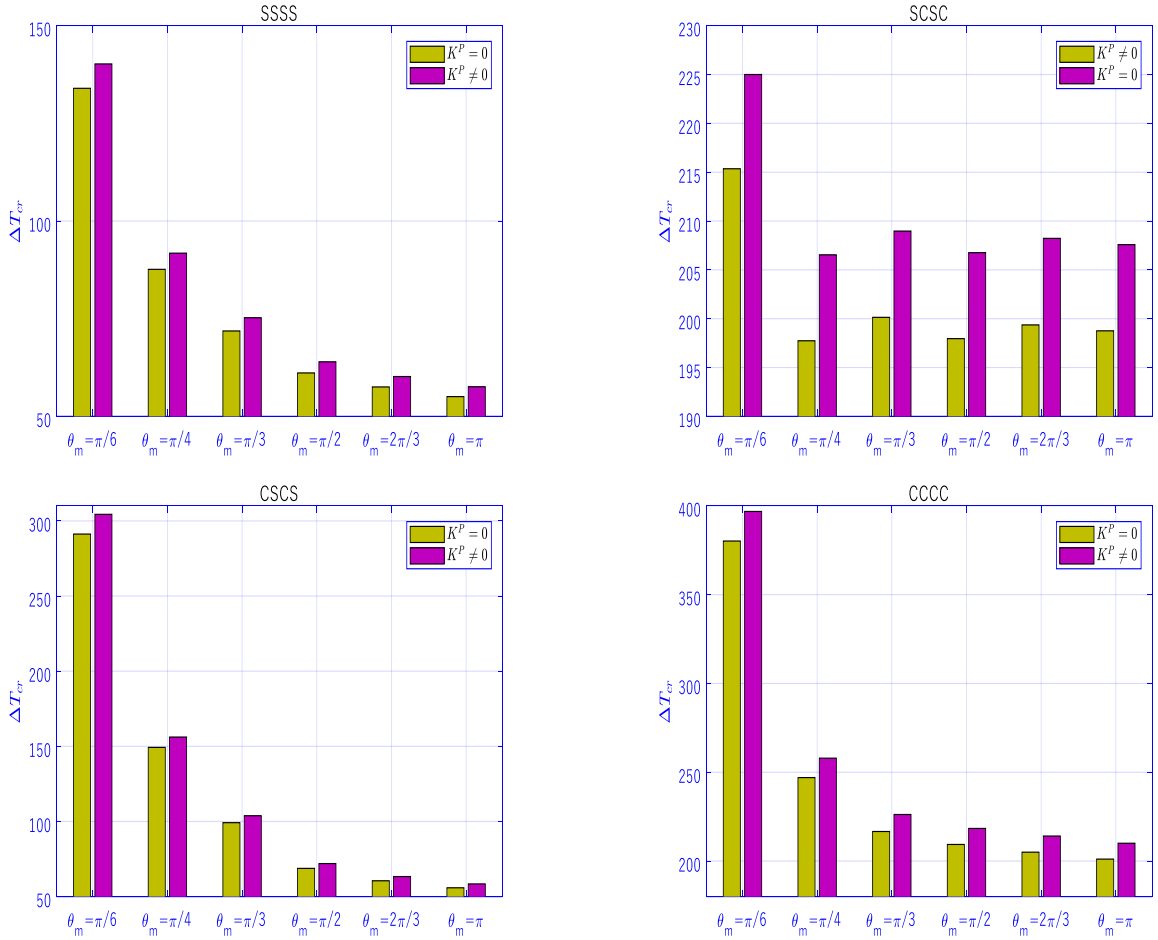

Fig. 3 Change in the critical temperature increase in buckling mode of annular sector plate as function of span angle considering $h = 0.1\,nm$, $R_i = 40h$, $R_o = 2R_i$, $n_r, n_\theta, n_z = 0.5$, $l = h$, $\mu = h$, $\emptyset_0 = 0.1\,(mV)$, and $A_P = \frac{A_T}{4}$

Table 7 An analysis of the DNN model's performance for critical temperature at different h/a ratios and RMSN values

h/a	Fit	Predicted		
		$RMSE_{Train}$ = 0.19	$RMSE_{Train}$ = 0.21	$RMSE_{Train}$ = 0.25
1/20	35.9424	45.1238	39.456	36.2304
1/15	52.0704	59.2082	53.3422	52.4344
1/13	69.3504	82.2182	74.2717	69.1523
1/10	81.1008	91.8328	84.6605	80.928
1/8	91.9296	103.968	97.1182	92.0632

Table 8 Performance of the DNN model's performance for critical temperature is evaluated across several values of R^2 and *h/a*

h/a	Fit	Predicted		
		$RMSE_{Train}$ = 0.19	$RMSE_{Train}$ = 0.21	$RMSE_{Train}$ = 0.25
1/20	34.0992	44.9856	38.0805	34.5254
1/15	44.928	56.5125	49.6466	45.292
1/13	56.448	68.1684	60.2381	56.8742
1/10	70.272	80.5432	74.0782	70.4678
1/8	94.464	107.71	99.4222	94.623

$$R^2 = \frac{\sum_{i=1}^{N}(o_i - o_{avg})^2 - \sum_{i=1}^{N}(o_i - y_i)^2}{\sum_{i=1}^{N}(o_i - o_{avg})^2}, \tag{38a}$$

$$RMSE = \sqrt{\frac{1}{N}\sum_{i=1}^{N}(O_i - y_i)^2}, \tag{38b}$$

This section investigates the effects of R^2 and RMSE on the results using Tables 7 and 8. A response with higher RMSE and R^2 parameter values might be assumed to be more accurate. Selecting 483 samples, RMSE=0.25, R^2=0.8351, and other results is very beneficial.

Tables 7 and 8 show that for both the numerical and DNN approaches, the structure's critical temperature increases as the curvature factor increases.

6. Conclusions

This study provides a comprehensive analysis of the electro-thermal buckling behavior of multi-directional poroelastic NEMS used as temperature sensors in airplanes. The research emphasizes the critical role of electro-thermal

loads in influencing the stability and performance of these advanced sensors. By employing advanced shear deformation theories and the generalized differential quadrature method (GDQM), the study accurately models the complex interactions within the NEMS, considering various boundary conditions and geometric configurations. It is for the first time that linear buckling performance of nano-scale annular functionally graded plate structures integrated with piezoelectric layers under electrical and extreme thermal loadings with a novel four-variable refined quasi-3D sinusoidal shear deformation theory (RQ-3DSSDT) is investigated. In this regard, piezoelectric layers are placed on a disk made of metal matrix composite with graded properties in three radials, thickness and circumferential directions. The grading properties obey the power-law distribution. The whole structure is embedded in thermal environment. To model the mechanical behavior of the structure, a novel four-variable refined quasi-3D sinusoidal shear deformation theory (RQ-3DSSDT) is engaged in obtaining displacement field in the whole structure. In addition, nonlocal strain gradient theory (NSGT) is used to correlate stress tensor to strain tensor. The equilibrium equations of the structure are extracted employing minimum virtual work principle and solved by the two-dimensional discrete singular convolution method (2D-DSCM). The validity of the results is examined by comparing to a similar problem published in literature. The results of the buckling behavior of the structure in different boundary conditions are presented based on the critical temperature rise and critical external voltage.

Acknowledgment

The authors extend their appreciation to the Deanship of Research and Graduate Studies at King Khalid University for funding this work through Large Research Project under grant number RGP2/291/45.

Funding

This study was funded by Chongqing Technology Innovation and Application Development Plan Project (CSTB2024TIAD-CYKJCXX0033).

References

Al-shujairi, M. and Mollamahmutoğlu, Ç. (2018), "Buckling and free vibration analysis of functionally graded sandwich micro-beams resting on elastic foundation by using nonlocal strain gradient theory in conjunction with higher order shear theories under thermal effect", *Compos. Part B Eng.*, **154**, 292-312. https://doi.org/10.1016/j.compositesb.2018.08.103.

Burdess, J.S. and Fawcett, J.N. (1992), "Experimental Evaluation of a Piezoelectric Actuator for the Control of Vibration in a Cantilever Beam", *Proceedings of the Institution of Mechanical Engineers, Part I: Journal of Systems and Control Engineering*, **206**(2), 99-106. https://doi.org/10.1243/PIME_PROC_1992_206_315_02.

Chen, C., Yang, H., Song, K., Liang, D., Zhang, Y. and Ni, J. (2023), "Dissolution feature differences of carbonate rock within hydro-fluctuation belt located in the Three Gorges Reservoir Area", *Eng. Geol.*, **327**, 107362. https://doi.org/10.1016/j.enggeo.2023.107362.

Chen, D., Yang, J. and Kitipornchai, S. (2017), "Nonlinear vibration and postbuckling of functionally graded graphene reinforced porous nanocomposite beams", *Compos. Sci. Technol.*, **142**, 235-245. https://doi.org/10.1016/j.compscitech.2017.02.008.

Chung, M., Lee, H.J., Kang, Y.C., Lim, W.B., Kim, J.H., Cho, J.Y., Byun, W., Kim, S.J. and Park, S.H. (2012), "Experimental study on dynamic buckling phenomena for supercavitating underwater vehicle", *Int. J. Naval Arch. Ocean Eng.*, **4**(3), 183-198. https://doi.org/10.2478/IJNAOE-2013-0089.

Civalek, Ö. (2017), "Free vibration of carbon nanotubes reinforced (CNTR) and functionally graded shells and plates based on FSDT via discrete singular convolution method", *Compos. Part B Eng.*, **111**, 45-59. https://doi.org/10.1016/j.compositesb.2016.11.03.

Drai, A., Daikh, A.A., Belarbi, M.O., Houari, M.S.A., Aour, B., Hamdi, A. and Eltaher, M.A. (2023), "Bending of axially functionally graded carbon nanotubes reinforced composite nanobeams", *Adv. Nano Res.*, **14**(3), 211-224. https://doi.org/10.12989/anr.2023.14.3.211.

Ebrahimi, F., Hashemabadi, D., Habibi, M. and Safarpour, H. (2020), "Thermal buckling and forced vibration characteristics of a porous GNP reinforced nanocomposite cylindrical shell", *Microsyst. Technol.*, **26**(2), 461-473. https://doi.org/10.1007/s00542-019-04542-9.

Eghbali, M. and Hosseini, S.A. (2024), "An accurate analytical exploration for dynamic response of thermo-electric CNTRC beams under driving harmonic and constant loads resting on Pasternak foundation", *Adv. Nano Res.*, **16**(6), 549-564. https://doi.org/10.12989/anr.2024.16.6.549

Esen, I., Alazwari, M.A., Almitani, K.H., Eltaher, M.A. and Abdelrahman, A. (2023), "Dynamic vibration response of functionally graded porous nanoplates in thermal and magnetic fields under moving load", *Adv. Nano Res.*, **14**(5), 475. https://doi.org/10.12989/anr.2023.14.5.475

Feng, Y., Mohammadi, M., Wang, L., Rashidi, M. and Mehrabi, P. (2021), "Application of artificial intelligence to evaluate the fresh properties of self-consolidating concrete", *Materials*, **14**(17), 4885. https://doi.org/10.3390/ma14174885.

Firouzianhaji, A., Usefi, N., Samali, B. and Mehrabi, P. (2021), "Shake table testing of standard cold-formed steel storage rack", *Appl. Sci.*, **11**(4), 1821. https://doi.org/10.3390/ma14174885.

Ghazwani, M.H., Alnujaie, A., Van Vinh, P. and Tounsi, A. (2024), "A quasi-3D nonlocal theory for free vibration analysis of functionally graded sandwich nanobeams on elastic foundations", *Adv. Nano Res.*, **16**(3), 313-324.

Gholami, R. and Ansari, R. (2017), "A unified nonlocal nonlinear higher-order shear deformable plate model for postbuckling analysis of piezoelectric-piezomagnetic rectangular nanoplates with various edge supports", *Compos. Struct.*, **166**, 202-218. https://doi.org/10.1016/j.compstruct.2017.01.045

Han, S., Zheng, D., Mehdizadeh, B., Nasr, E.A., Khandaker, M.U., Salman, M. and Mehrabi, P. (2023a), "Sustainable design of self-consolidating green concrete with partial replacements for cement through neural-network and fuzzy technique", *Sustainability*, **15**(6), 4752. https://doi.org/10.3390/su15064752.

Han, S., Zhu, Z., Mortazavi, M., El-Sherbeeny, A.M. and Mehrabi, P. (2023b), "Analytical assessment of the structural behavior of a specific composite floor system at elevated temperatures using a newly developed hybrid intelligence method", *Buildings*, **13**(3), 799. https://doi.org/10.3390/buildings13030799.

Hirao, Y., Wan, W., Kanoulas, D. and Harada, K. (2023), "Body extension by using two Mobile manipulators", *Cyborg Bionic*

Syst., **4**, 0014. https://doi.org/10.34133/cbsystems.0014
Hou, Y., Wei, G. and Xiang, Y. (2005), "DSC-Ritz method for the free vibration analysis of Mindlin plates", *Int. J. Numer. Meth. Eng*., **62**(2), 262-288. https://doi.org/10.1002/nme.1186
Hu, D., Sun, H., Mehrabi, P., Ali, Y.A. and Al-Razgan, M. (2023), "Application of artificial intelligence technique in optimization and prediction of the stability of the walls against wind loads in building design", *Mech. Adv. Mater. Struct*., 1-18. https://doi.org/10.1080/15376494.2023.2206208.
Kargarnovin, M.H., Najafizadeh, M.M. and Viliani, N.S. (2007), "Vibration control of a functionally graded material plate patched with piezoelectric actuators and sensors under a constant electric charge", *Smart Mater. Struct*., **16**(4), 1252-1259. https://doi.org/10.1088/0964-1726/16/4/037.
Ke, L.L. and Wang, Y.S. (2014), "Free vibration of size-dependent magneto-electro-elastic nanobeams based on the nonlocal theory", *Physica E*, **63**, 52-61. https://doi.org/10.1016/j.physe.2014.05.002.
Lim, C., Li, Z. and Wei, G. (2005), "DSC-Ritz method for high-mode frequency analysis of thick shallow shells", *Int. J. Numer. Meth. Eng*., **62**(2), 205-232. https://doi.org/10.1002/nme.1179.
Lim, C., Zhang, G. and Reddy, J. (2015), "A higher-order nonlocal elasticity and strain gradient theory and its applications in wave propagation", *J. Mech. Phys. Solids*, **78**, 298-313. https://doi.org/10.1016/j.jmps.2015.02.001.
Liu, B., Yang, H. and Karekal, S. (2020), "Effect of water content on argillization of mudstone during the tunnelling process", *Rock Mech. Rock Eng*., **53**, 799-813. https://doi.org/10.1007/s00603-019-01947-w.
Liu, J., Mohammadi, M., Zhan, Y., Zheng, P., Rashidi, M. and Mehrabi, P. (2021), "Utilizing artificial intelligence to predict the superplasticizer demand of self-consolidating concrete incorporating pumice, slag, and fly ash powders", *Materials*, **14**(22), 6792. https://doi.org/10.3390/ma14226792.
Liu, R., Li, H., Khadimallah, M.A. and Safarpour, M. (2022), "Three-dimensional poroelasticity solution of sandwich, cylindrical, open, functionally graded composite panels under multi-directional initial stress: semi-numerical modeling", *Arch. Civil Mech. Eng*., **22**(1), 1-42. https://doi.org/10.1007/s43452-021-00337-w.
Lv, Y., Wei, J., Huang, Z., Zhang, Z., Ding, S., Zhang, C., Wang, W., Xu, K., Xu, R. and Wang, L. (2024), "Superelastic bamboo fiber-based spongy aerogel for flexible piezoresistive sensors with wide response range and high sensitivity", *Chem. Eng. J*., **488**, 151053. https://doi.org/10.1016/j.cej.2024.1510.
Mehrabi, P., Honarbari, S., Rafiei, S., Jahandari, S. and Alizadeh Bidgoli, M. (2021), "Seismic response prediction of FRC rectangular columns using intelligent fuzzy-based hybrid metaheuristic techniques", *J. Ambient Intell. Human. Comput*., **12**, 10105-10123. https://doi.org/10.3390/ma14174885.
Mehrabi, P., Shariati, M., Kabirifar, K., Jarrah, M., Rasekh, H., Trung, N.T., Shariati, A. and Jahandari, S. (2021), "Effect of pumice powder and nano-clay on the strength and permeability of fiber-reinforced pervious concrete incorporating recycled concrete aggregate", *Constr. Build. Mater*., **287**, 122652. https://doi.org/10.3390/ma14174885.
Moayedi, H., Aliakbarlou, H., Jebeli, M., Noormohammadiarani, O., Habibi, M., Safarpour, H. and Foong, L.K. (2020), "Thermal buckling responses of a graphene reinforced composite micropanel structure", *Int. J. Appl. Mech*., **12**(1), 2050010. https://doi.org/10.1142/S1758825120500106.
Pietrzakowski, M. (2008), "Piezoelectric control of composite plate vibration: Effect of electric potential distribution", *Comput. Struct*., **86**(9), 948-954.
Qiu, Y. (2019), "Estimation of tail risk measures in finance: Approaches to extreme value mixture modeling", Johns Hopkins University.
Qiu, Y. and Wang, J. (2024), "A Machine Learning Approach to Credit Card Customer Segmentation for Economic Stability", *Proceedings of the 4th International Conference on Economic Management and Big Data Applications*, ICEMBDA 2023, October 27-29, Tianjin, China.
Reddy, J. and Chin, C. (1998), "Thermomechanical analysis of functionally graded cylinders and plates", *J. Therm. Stress*., **21**(6), 593-626. https://doi.org/10.1080/01495739808956165.
Reddy, J.N. (2003), *Mechanics of Laminated Composite Plates and Shells: Theory and Analysis*, CRC press.
Safarpour, H., Esmailpoor Hajilak, Z. and Habibi, M. (2019), "A size-dependent exact theory for thermal buckling, free and forced vibration analysis of temperature dependent FG multilayer GPLRC composite nanostructures restring on elastic foundation", *Int. J. Mech. Mater. Des*., **15**(3), 569-583. https://doi.org/10.1007/s10999-018-9431-8.
Safarpour, H., Ghanbari, B. and Ghadiri, M. (2019), "Buckling and free vibration analysis of high speed rotating carbon nanotube reinforced cylindrical piezoelectric shell", *Appl. Math. Modell*., **65**, 428-442. https://doi.org/10.1016/j.apm.2018.08.028.
Sepahi, O., Forouzan, M.R. and Malekzadeh, P. (2011), "Thermal buckling and postbuckling analysis of functionally graded annular plates with temperature-dependent material properties", *Mater. Des*., **32**(7), 4030-4041. https://doi.org/10.1016/j.matdes.2011.03.063.
Shahsiah, R. and Eslami, M. (2003), "Thermal buckling of functionally graded cylindrical shell", *J. Therm. Stress*., **26**(3), 277-294. https://doi.org/10.1080/713855892.
Shivashankar, P. and Gopalakrishnan, S. (2020), "Review on the use of piezoelectric materials for active vibration, noise, and flow control", *Smart Mater. Struct*., **29**(5), 053001. https://doi.org/10.1088/1361-665x/ab7541.
Song, K., Yang, H., Liang, D., Chen, L. and Jaboyedoff, M. (2024), "Step-like displacement prediction and failure mechanism analysis of slow-moving reservoir landslide", *J. Hydrol*., **628**, 130588. https://doi.org/10.1016/j.jhydrol.2023.130588.
Sun, J., Zhou, L., Geng, B., Zhang, Y. and Li, Y. (2024), "Leg state estimation for quadruped robot by using probabilistic model with proprioceptive feedback", *IEEE/ASME T. Mechatron*., Early Access. https://doi.org/10.1109/TMECH.2024.3421251.
Taheri, E., Firouzianhaji, A., Mehrabi, P., Vosough Hosseini, B. and Samali, B. (2020), "Experimental and numerical investigation of a method for strengthening cold-formed steel profiles in bending", *Appl. Sci*., **10**(11), 3855. https://doi.org/10.3390/app10113855.
Taheri, E., Firouzianhaji, A., Usefi, N., Mehrabi, P., Ronagh, H. and Samali, B. (2019), "Investigation of a method for strengthening perforated cold-formed steel profiles under compression loads", *Appl. Sci*., **9**(23), 5085. https://doi.org/10.3390/ma14174885.
Taheri, E., Mehrabi, P., Rafiei, S. and Samali, B. (2021), "Numerical evaluation of the upright columns with partial reinforcement along with the utilisation of neural networks with combining feature-selection method to predict the load and displacement", *Appl. Sci*., **11**(22), 11056. https://doi.org/10.3390/app112211056.
Thai, H.T. and Kim, S.E. (2013), "A simple quasi-3D sinusoidal shear deformation theory for functionally graded plates", *Compos. Struct*., **99**, 172-180. https://doi.org/10.1016/j.compstruct.2012.11.030.
Toghroli, A., Mehrabi, P., Shariati, M., Trung, N.T., Jahandari, S. and Rasekh, H. (2020), "Evaluating the use of recycled concrete aggregate and pozzolanic additives in fiber-reinforced pervious concrete with industrial and recycled fibers", *Constr. Build. Mater*., **252**, 118997. https://doi.org/10.3390/ma14174885.
Wang, C.M., Xiang, Y., Kitipornchai, S. and Liew, K.M. (1994),

"Buckling solutions for Mindlin plates of various shapes", *Eng. Struct.*, **16**(2), 119-127. https://doi.org/10.1016/0141-0296(94)90037-X.

Wang, K., Boonpratatong, A., Chen, W., Ren, L., Wei, G., Qian, Z., Lu, X. and Zhao, D. (2023), "The fundamental property of human leg during walking: linearity and nonlinearity", *IEEE T Neural Syst. Rehabil. Eng.*, **31**, 4871-4881.

Wang, Q. (2002), "On buckling of column structures with a pair of piezoelectric layers", *Eng. Struct.*, **24**(2), 199-205. https://doi.org/10.1016/S0141-0296(01)00088-8.

Wang, X., Zhang, R., Miao, Y., Wang, S. and Zhang, Y. (2024), "PI^2-based adaptive impedance control for gait adaption of lower limb exoskeleton", *IEEE/ASME T. Mechatron.*, Early Access. https://doi.org/10.1109/TMECH.2024.3370954.

Wei, G. (2001), "Vibration analysis by discrete singular convolution", *J. Sound Vib.*, **244**(3), 535-553. https://doi.org/10.1006/jsvi.2000.3507.

Wei, G., Zhao, Y. and Xiang, Y. (2001), "The determination of natural frequencies of rectangular plates with mixed boundary conditions by discrete singular convolution", *Int. J. Mech. Sci.*, **43**(8), 1731-1746. https://doi.org/10.1016/S0020-7403(01)0002.

Wu, H., Kitipornchai, S. and Yang, J. (2017), "Thermal buckling and postbuckling of functionally graded graphene nanocomposite plates", *Mater. Des.*, **132**, 430-441. https://doi.org/10.1016/j.matdes.2017.07.025.

Wu, J., Yang, Y., Mehrabi, P. and Nasr, E.A. (2023), "Efficient machine-learning algorithm applied to predict the transient shock reaction of the elastic structure partially rested on the viscoelastic substrate", *Mech. Adv. Mater. Struct.*, 1-25. https://doi.org/10.1080/15376494.2023.2183289.

Yang, H., Chen, C., Ni, J. and Karekal, S. (2023), "A hyperspectral evaluation approach for quantifying salt-induced weathering of sandstone", *Sci. Total Environ.*, **885**, 163886. https://doi.org/10.1016/j.scitotenv.2023.163886.

Yang, H., Ni, J., Chen, C. and Chen, Y. (2023), "Weathering assessment approach for building sandstone using hyperspectral imaging technique", *Heritage Sci.*, **11**(1), 70. https://doi.org/10.1186/s40494-023-00914-7.

Yang, H., Song, K. and Zhou, J. (2022), "Automated recognition model of geomechanical information based on operational data of tunneling boring machines", *Rock Mech. Rock Eng.*, 1-18. https://doi.org/10.1007/s00603-021-02723-5.

Zhang, C., Hu, H., Ma, Q. and Wang, N. (2023), "Computational thermal stability and critical temperature buckling of nano-system", *Adv. Nano Res.*, **14**(6), 575-590. https://doi.org/10.12989/anr.2023.14.6.575.

Zhang, C., Liu, Y., Zhang, Y., Ketabdar, A. and Xiang, H. (2024), "Study of educational management on performance of scholar in nano/micro-level composite", *Adv. Nano Res.*, **16**(6), 615-622. https://doi.org/10.12989/anr.2024.16.6.615

Zhang, S., Wang, C., Zhang, H. and Lin, H. (2024), "Collective dynamics of adaptive memristor synapse-cascaded neural networks based on energy flow", *Chaos, Solitons Fract.*, **186**, 115191. https://doi.org/10.1016/j.chaos.2024.115191.

Zhang, Y., Wang, Z., Tazeddinova, D., Ebrahimi, F., Habibi, M. and Safarpour, H. (2021), "Enhancing active vibration control performances in a smart rotary sandwich thick nanostructure conveying viscous fluid flow by a PD controller", *Waves Random Complex Med.*, 1-24. https://doi.org/10.1080/17455030.2021.1948627.

Zhao, Y. and Wei, G. (2002), "DSC analysis of rectangular plates with non-uniform boundary conditions", *J. Sound Vib.*, **255**(2), 203-228. https://doi.org/10.1006/jsvi.2001.4150.